Master of Science Thesis
HT2020

# Evaluation of internal dosimetry for 225-Ac using one single measurement based on 111-In imaging


Selma Curkic

Supervisors

Michael Ljungberg, Katarina Sjögreen-Gleisner and Johan Gustafsson

Medical Radiation Physics, Lund
Faculty of Science
Lund University
www.msf.lu.se

# Abstract

**Background and aim**: There is a high interest in determining the absorbed dose in tumors and organs for various radiotherapy cancer treatments. Due to limitations in today's methods of determining the patient specific absorbed dose it is usually not proceeded clinically. The methods are time consuming but also trying for patients, since it depends on several imaging procedures at different times during a time period of about seven days p.i. Therefore the aim of this thesis is to find a new method that is not as challenging for the clinic and patients, yet is as effective as the current one. The new method (1-point method) is based on single time point dosimetry for a newly developed therapy using the alpha emitting $^{225}$Ac with the help of $^{111}$In for imaging.

**Method**: The work was divided into two parts. The first one consisted of making time activity concentration curves (TACC), based on given biokinetic data, for each organ being examined. The curves were explained either as a bi-exponential curve with uptake or without uptake. Parameters given from these curves were then used to calculate the true time integrated activity concentrations (TIAC) used as reference data. Afterwards CT-based phantoms were created after real patient data, where data from five patients was used. By using the Monte-Carlo based program SIMIND, SPECT simulations were performed at four different time points for all phantoms to calculate the TIAC with the current method (4-point method), called test data. The 4-point method is based on fitting a curve to activities quantified from four imaging procedures at different time points over the course of a week, and then integrating it. For the second part, a derivation was made to find the optimal time point ($t_{opt}$) when the single SPECT/CT measurement should be made to still obtain reasonable results while minimizing the uncertainties. Derivation of $t_{opt}$ resulted in $t_{\text{opt}} = \frac{1}{\lambda^*_{Ac}}$, where $\lambda^*_{Ac}$ is the mean effective decay constant for each individual organ for $^{225}$Ac. Following this derivation different organs should have different optimal imaging times, since they have different biological decay constants. Therefore, simulations were performed at 96, 120 and 144 hours p.i. to test this theory. The TIAC's obtained were then compared to reference data and the test data calculated with the 4-point method. TIAC's for the 1-point method were given by integrating a mono-exponential curve based on the activity quantified from the single time point and a mean effective decay constant. Since $^{111}$In is our imaging radionuclide the TIAC's were first calculated for $^{111}$In and then re-calculated for $^{225}$Ac, except for the 1-point method where the TIAC's for $^{225}$Ac were given straight away.

**Results and conclusion**: The results show that, for majority of the organs, the test data received with the 1-point method deviates with -4 % to 12 % from reference data for later measurements p.i. while the kidneys deviate with around 31 %. One reason being their low activity concentration around 144 hours p.i. For earlier p.i. measurements it lies around 6 % to 12 %, and for the kidneys 27 %. Thus organs with later $t_{opt}$ had lower uncertainties at 144 hours p.i. Those with an earlier optimal imaging time, such as the kidneys, had lower uncertainties at 96 hours p.i. Similar percentages are given when deviations between the 4-point method test data and reference data are produced. Results also show that the TIAC's received with the 1-point method test data are overestimated when compared directly to the 4-point method test data. For later p.i. measurements they deviate with about 1 % to 5 %, while for earlier p.i. measurements they deviate with about 0 % to 13 %. Therefore, depending on what accuracy one is searching for and the resources available to determine the absorbed doses, both the 4-point method and the 1-point method are successful.

# Förenklad metod för att bestämma den absorberade dosen

Dosimetri är läran om hur strålning deponerar eller frigör sin energi i vävnad samt hur mängden energi som avgetts kan bestämmas genom mätning eller beräkning. Detta används vid t.ex. interna strålbehandlingar där man genom att injicera radioaktivitet vill behandla vissa typer av tumörer och då vill undersöka hur stor mängd av radioaktiviteten man injicerat som kommer tas upp och bestråla olika organ. Genom att diagnostisera kan vi se hur radioaktiviteten har fördelat sig i kroppen, detta kan utföras med en single photon emission computer tomography (SPECT) som utanför kroppen mäter aktivitetsfördelningen personen har innanför kroppen. Den storhet man använder sig av för att koppla cancer behandlingar till den radiobiologiska effekten som strålningen orsakar är ofta absorberad dos, vilken definieras som deponerad energi per massenhet. Att bestämma den absorberade dosen är tidskrävande och påfrestande för klinikerna, då det kräver att flera SPECT-bildtagningar sker under en viss tidsperiod. Därför är syftet med det här arbetet att förenkla metoden för att bestämma den absorberade dosen, genom att enbart basera den på en enda SPECT-bildtagning.

Detta arbete är baserat på en typ av alfa-terapi, där man kan behandla tumörer genom att binda en alfa-strålare till en antikropp som i sin tur kan binda till olika tumörer. En alfa-strålare är en typ av radionuklid som sönderfaller genom att emittera en alfa-partikel. I det här fallet används $^{225}$Actinium ($^{225}$Ac) för att leverera alpha-partiklarna. Alfa-partiklar är duktiga på att orsaka dubbelsträngsbrått i vårt DNA, vilket är ett effektivt sätt att döda celler på om inte cellen lyckas reparera dubbelsträngsbråttet. På så sätt är det viktigt att se till att så mycket som möjligt av den injicerade radioaktiviteten bestrålar enbart tumörerna och så lite som möjligt bestrålar frisk vävnad, då vi inte vill orsaka någon skada på cellerna i våra friska organ. Alfa-partiklar kommer avge all sin energi i vävnaden den passerar igenom, därför kan inte SPECT-kameran mäta fördelningen av $^{225}$Ac. Vi får istället injicera ytterligare en radionuklid som sönderfaller med gammafotoner, i det här fallet använde vi oss av $^{111}$Indium ($^{111}$In). Gammafotoner avger oftast inte sin energi i vävnaden där sönderfallet skedde utan kan ta sig utanför kroppen vilket gör att vi kan mäta på det.

Genom att mäta vid flera olika tidpunkter över en viss tid kan vi bestämma hur mycket radioaktivitet vi har kvar i kroppen vid de olika tillfällena. Mängden dos ett organ får ta beror bland annat på hur länge det blir bestrålat. Desto fler mättidpunkter man har desto mer korrekt blir dosberäkningen, då vi verkligen kan se hur mycket radioaktivitet organen tar upp och hur länge det är kvar i organet. Genom att anpassa en kurva till dessa mättidpunkter får vi en beskrivning av det specifika organets upptag och utsöndring av radioaktiviteten. Målet är dock att med en enda mättidpunkt kunna bestämma det ovannämnda och fortfarande få liknande resultat. Det går att hitta när mättidpunkten ska ske så att beräkningen av den absorberade dosen som görs baserat på en tidpunkt stämmer överens med den absorberade dosen baserat på flera tidpunkter.

Resultatet av det här arbetet visar att det går att beräkna absorberad dos med en enda mättidpunkt. Genom att ta fram den optimala tidpunkten när mätningen ska ske och sedan beräkna dosen från den får man liknande resultat som om den absorberade dosen beräknats med flera mättidpunkter. Självfallet är resultaten bättre då flera mättidpunkter används, men med tanke på hur mycket resurser som besparas med den nya metod kan den fortfarande vara lyckad och användbar.

# Contents

## Abbrevation

**TIAC**: Time Integrated Activity Concentration

**TACC**: Time Activity Concentration Curve

**VOI**: Volume of Interest

**ROI**: Region of Interest

**SPECT**: Single Photon Emission Computed Tomography

**IA**: Injected Activity

**ESSE**: Effective Scatter Source Estimation

**OS-EM**: Ordered Subset Expectation Maximization

**ML-EM**: Maximum Likelihood Expectation Maximization

**CT**: Computer Tomography

**p.i.**: post injection

$^{225}$**Ac**: $^{225}$Actinium

$^{111}$**In**: $^{111}$Indium

**PVE**: Partial volume effect

**PVC**: Partial volume correction

**CDR**: Collimator detector response

# 1 Introduction

## 1.1 Background and aim

The accuracy of determining the absorbed radiation dose in normal tissue and tumours is key for all radiotherapy. It is of high importance to know if the therapies are efficient or if they only do harm to normal tissue. Although in radionuclide therapy the procedure for determining the absorbed dose carries different challenges which limits its application in routine practice [1]. There is a clinical trial being proceeded for a rather new targeted alpha radioimmunotherapy using the radiopharmaceutical $^{225}$Ac-FPI-1434, with the help of $^{111}$In-FPI-1547 for imaging. During the trial the multiple time points method is used to estimate the absorbed doses for the lungs, kidneys, spleen, liver and red bone marrow. Where the main objectives are the kidneys and bone marrow. The current method (4-point method) for determining the dose a tissue or organ receives depends on four post injection (p.i.) planar images and two SPECT/CT procedures to be completed. Thus, the 4-point method is time consuming and challenging for the clinics implementing it, but also for the patients. Therefore, the aim of this project is to determine whether we can calculate the absorbed doses using the single time point dosimetry method (1-point method) while still obtaining valid results.

The interest in simplifying the dosimetry calculations have grown bigger in the last couple of years and research groups such as Hänscheid et. al. and Madsen et. al. have provided options to how this can be proceeded. Hänsheid et. al. studied the radiopharmaceutical $^{177}$Lu-DOTATATE/-TOC where they concluded that a quantitative measurement 4 days p.i. is optimal to use if one wants to determine the doses with the use of one single measurement point. The results showed that $^{177}$Lu accumulating tissues showing mono-exponential decay with effective half-lives between 38 and 128 hours provided errors in the dose calculations with less than 10 %. [2] While Madsen et. al. used a more general approach for both mono-exponential and bi-exponential cases. They derived an optimal sampling time point for both cases, as to when the measurement should be proceeded for minimum errors. For the majority of their dose estimates they were in the range of 10 % of the actual dose. All their calculations were based on $^{90}$Y-DOTATOC, where they concluded that the method requires prior knowledge about population averaged tracer kinetic parameters. They predicted an optimal sampling time at 50 hours for $^{90}$Y-DOTATOC and results showed minimal errors for single point dose estimates at 48 hours p.i. [3]

Both of these research groups based their dose calculations and error estimations on their imaging radionuclide, thus finding optimal sampling times for that particular one. In this thesis there is no interest in calculating doses for the imaging radionuclide, but instead using it to obtain dose calculations for the alpha-emitting $^{225}$Ac. Hence, the goal is to see if it is possible to determine the internal dose of $^{225}$Ac using a single SPECT measurement of $^{111}$In, and if that is the case, when should that single measurement take place for optimal dose calculations?

# 2 Theory

## 2.1 Targeted alpha radioimmuotherapy with $^{225}$Ac

The therapy this thesis is based on is a part of the targeted radioimmunotherapy. Alpha-particle emitting nuclides have presented new possibilities thanks to increased availability and improved radiochemistry. Because alpha-particles have a high linear energy transfer (LET), in the order of 100 kev/$\mu$m, they can to a significant extent produce more lethal double strand DNA-breaks per alpha particle track compared to a beta-particle. $^{225}$Ac mostly decays via alpha-particles and the key property of the alpha-decay are their limited range in tissue of a few cell diameters, dense radiation damage along each particle track due to high LET, a 10 day half-life and its four net alpha particles emitted per decay. $^{225}$Ac occurs naturally in association with uranium radionuclides and can be obtained either from the decay of $^{233}$U or from the neutron transmutation of $^{226}$Ra by successive n, $\gamma$ capture decay reactions via $^{227}$Ac, $^{228}$Th to $^{229}$Th. [4]

The molecule engineered to deliver alpha particles to cancer cells is [$^{225}$Ac]-FPI-1434. It was created by combining an humanized monoclonal antibody for an established cancer biomarker, insuling-like growth factor-1 receptor (IGF-1R), to create a targeted alpha therapy which can be used in various tumour types. IGF-1R is a well established tumour target found on many different types of cancer cells. The biomarker is used simply as a way to identify and target the tumour to deliver the alpha emitting payload. As part of the screening process for the trial every patient is administered a single injection of FPI-1547, the imaging analogue of FPI-1434, which contains of $^{111}$In instead of $^{225}$Ac. [5]

Following image displays the decay scheme of $^{225}$Ac and its daughter nuclides. It also shows that most of them decay via alpha or beta decay.

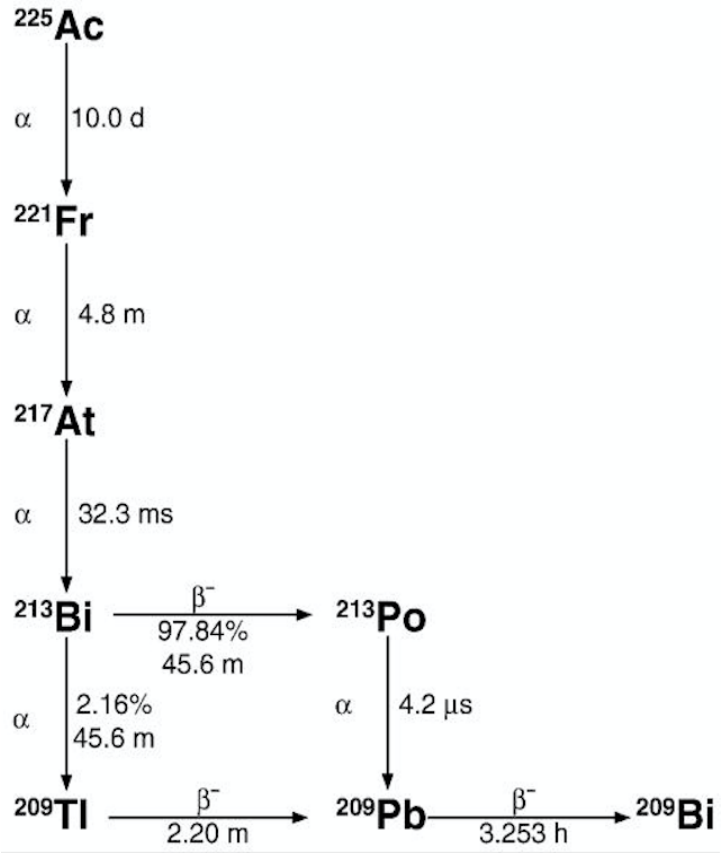


Figure 1: Decay scheme of $^{225}$Ac.[6]

## 2.2 Diagnostic radionuclide $^{111}$In

Since diagnostics can't be made on alpha-emitters due to their large amount of energy deposited in each decay, high LET, lead to a low amount of administered activity. Although there are photon emissions in the decay, the total amount of emitted photons are too few to enable imaging, particularly quantitative imaging. Thus, injection of a gamma-emitting tracer is needed. $^{111}$In is widely used for diagnostic and therapy purposes and is a radionuclide that disintegrates by 99.99 % with electron capture and has a halflife of 2.8 days. [7] It also disintegrates via gamma transition, where it emits by 99.995 % a gamma photon of 171 keV and by 100 % a gamma photon of 245 keV.[8] It is produced in a cyclotron through the following reaction: $^{111}$Cd (p,n)$^{111}$In. [9] Due to the rather small halflife of $^{111}$In compared to the halflife of $^{225}$Ac there is a possibility that imaging with $^{111}$In will not result in a completely accurate description of the organ kinetics. As of now it is assumed that the kinetics follow a bi-exponential behavior because of what is seen when imaging with $^{111}$In. Although there might be a third phase that occurs much later which we cannot see due to the small amount of $^{111}$In left when this phase starts. Following image displays the decay of $^{111}$In.

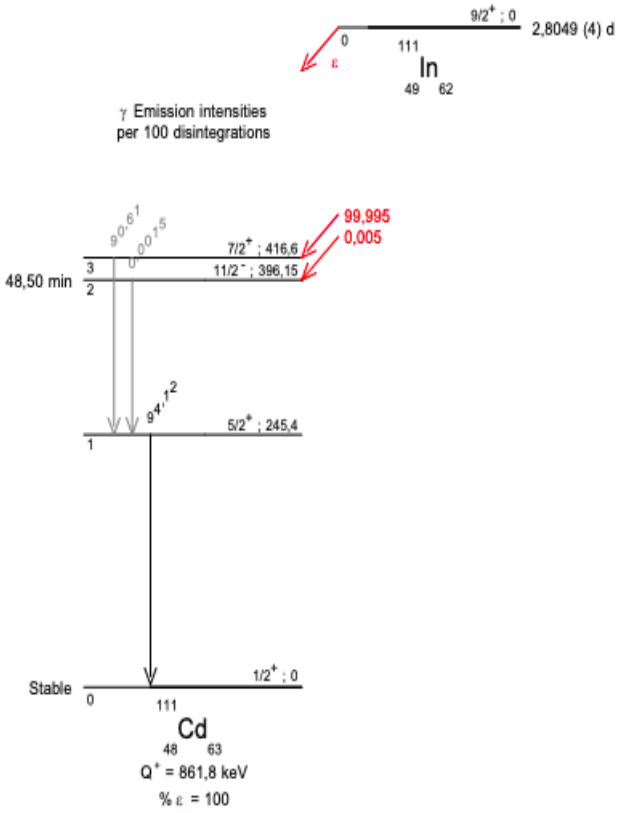


Figure 2: Decay scheme of $^{111}$In taken from LNHB.[8]

## 2.3 Internal dose calculations

The fundamental quantity for coupling cancer treatments to the radiobiological effect using radiation is often the absorbed dose. The absorbed dose, D, is defined as the mean energy imparted, d$\varepsilon$ to the volume with mass dm, according to following equation: [10]

$$D = \frac{d\varepsilon}{dm}. \tag{1}$$

The MIRD formalism gives a framework for the calculation of the absorbed dose to a target region. The absorbed dose is calculated as a product between the time integrated activity in a source region $\tilde{A}(r_s)$ and the S-value, D=$\tilde{A}(r_s) \cdot S$. A source or a target region can be any well-defined volume such as the whole body or an organ/tissue. The number of decays in the source region, also called the time integrated activity, is calculated as the area under the curve which describes the source region activity as a function of time post injection (p.i.) of the administered activity. The time integrated activity is usually calculated from the time of the injection of the activity until infinity, since that is most often taken as when the exposure ends.[11] The time integrated activity is thus

$$\tilde{A}(r_s,t) = \int_0^\infty A(r_s,t)dt. \tag{2}$$

The S-value is defined as a product between the energy emitted $E_i$, the probability for that energy to be emitted $n_i$ and the absorbed fraction $\phi$ and the mass of the target region $m(r_T)$. The absorbed fraction, $\phi$ is defined as the fraction of the emitted energy which is absorbed in the target region and has a value between 0 and 1. It is dependent on the shape, size and mass of the source and target regions, but also of the distance and type of material between the source and target region and lastly the type of radiation emitted from the source and the energy of the radiation. The S-value thus sums up to be

$$S(r_T \leftarrow r_{s,t}) = \frac{1}{m(r_T)} \sum_i \Delta_i \cdot \phi(r_t \leftarrow r_s, E_i), \tag{3}$$

where $\Delta_i = E_i \cdot n_i$. The total mean absorbed dose to a target region is given by summing the separate contribution from each source region

$$D(r_T) = \frac{1}{m(r_T)} \sum_{r_s} \Big[ \int_0^\infty A(r_s,t)dt \sum_t \Delta_i \cdot \phi(r_t \longleftarrow r_s, E_i) \Big] = \sum_{r_s} \tilde{A}(r_s) \cdot S(r_T \leftarrow r_s, E_i). \tag{4}$$

The S-values are specific for each radionuclide and source-target combinations. For calculations of the mean absorbed dose where all the emitted energy is assumed to be locally absorbed the calculation of organ-or tissue-specific S values are avoided, meaning when $\phi$=1. The absorbed dose calculation (self-absorbed dose) can then be simplified to [12]

$$D(r_s \leftarrow r_s) = \frac{\tilde{A}(r_s) \cdot \Delta}{m(r_s)} = \frac{\tilde{C}(r_s) \cdot \Delta}{\rho}, \tag{5}$$

where $\tilde{C}$ is the time integrated activity concentration. The activity as a function of time within a source region can be described as a sum of exponential functions

$$A(t) = \sum_j A_j \cdot e^{-t(\lambda_p + \lambda_b)}, \tag{6}$$

where j denotes the number of exponentials, $A_j$ the intial activity of the j:th exponential, $\lambda_p$ the physical decay constant of the radionuclide, $\lambda_b$ is the biological decay constant and t the time after the administration of the radionuclide. The decay constant for a certain radionuclide and biological decay constant can be combined into an effective decay constant where [11]

$$\lambda_e = \lambda_p + \lambda_b. \tag{7}$$

## 2.4 Single Photon Emission Computer Tomography (SPECT)

To determine the absorbed dose one has to determine the time integrated activity concentration as explained above. To do so the activity in a source target has to be quantified over time. This can be done by first imaging the activity distribution and then reconstructing those images. The distribution can be determined by a gamma camera or a single photon emission computer tomography (SPECT). The idea behind the scintillation camera or gamma camera is that it is a device which measures 2D images of a radionuclide distribution by detecting emitted photons in vivo. Although events coming from photons emitted at different source depths will be layered over and the source depth will be superimposed. This is solved by obtaining the 3D information of the

source by measuring projections in different views around the patient and using a reconstruction algorithm to display it.[13]

In radionuclide therapy the scintillation camera is the most commonly used device for in vivo activity distributions. [10] The camera head is built in such a way that the first part the photons see is the collimator. A collimator in its simplest form is a lead sheet with many parallel holes and photons that have a parallel incidence angle to the collimator are transmitted and interact within the crystal, while the rest are attenuated in the collimator. The second part they see is the crystal, usually a Thallium doped Sodium Iodine (NaI(Tl)). The camera works in such a way that gamma photons emitted in the radioactive decay interact with the scintillation crystal when reaching it. They will then transfer their energy to electrons who will interact with atoms and excite them. The atoms will de-excite and thus emit visible light. The light will then take its way to a photocathode or a light guide. Here the light will interact with the cathode, transfer its energy to electrons in the material which will be released and make their way in to the photomultiplier tube (PMT). The PMT contains of several dynodes, angled towards eachother. The primary electrons from the photocathode will make their way to the first dynode where more electrons will be released. Since the dynodes are angled they will be accelerated towards the second dynode where more electrons are released and so on. At the end the number of electrons will be magnified with a certain factor and hence our signal from the attenuated photon is readable. [10]

At the end of the PMT there is an anode which collects the amplified electrons and outputs the electron current to an external circuit. The shape of this output signal is a rapid rising peak with a slow decaying tail, which needs to be shaped. The signal has to have a certain pulse decrease time to be able to be fed into the amplifier. Using a pre-amplifier with a resistor-capacitor circuit the signal from the PMT is shaped. The signal also has a high impedance value, which also has to be matched with the rest of the electronics before the amplifier can deal with it. The role of the amplifier is then to amplify and shape the signal further. The signal is amplified to prevent further processing by the rest of the electronics. Further shaping is made by eliminating the tail of the signal and giving each signal its width and amplitude to prevent them from overlapping with other signals. The signal is then further processed by the pulse height analyzer (PHA) which measures the signals pulse height amplitude and compare them to preset values stored within it. Some of the gamma photons will lose some or most of their energy on their way to or in the crystal. Mostly they will scatter and lose their energy within the patient. This type of scatter will dominate the spectrum and thus degrade the image quality and contrast resolution. The output signal will therefore not be a sharp peak line, but a distribution of pulse heights with one or more peak lines which represent the energies of the measured photons. Therefore, the role of the PHA is to apply lower and upper voltage discriminators. Output signals from the amplifier have a range of height and by setting a lower discriminator to a level that diminishes all lower values only the upper ones will be recorded. [14]

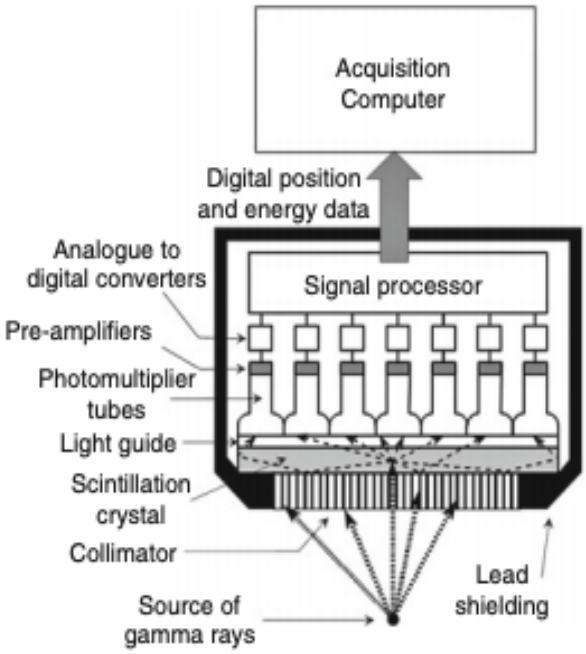


Figure 3: Image displaying the order of most of the components in a gamma camera head. [15]

The gamma camera is designed to provide acceptable detection efficiency while maintaining reasonable intrinsic spatial resolution for an energy range of 100-200 keV. [16] Spatial resolution refers to a cameras ability to spatially resolve two sources of radioactivity as separate items. For scintillation cameras the spatial resolution can be described as a point spread function (PSF) and is often modelled as a Gaussian function with a certain full width at half maximum (FWHM) which is distance dependent. This effect will also result in a partial volume effect (PVE), meaning that a pixel will include a mixture of signals coming from different sources. Part of the activity from the structure will thus be detected outside of the VOI drawn around it, called spill-out. This also means that the activity from the structures around the structure of interest will spill-in to the structure of interest. Even if we had ideal spatial resolution PVEs would still occur due to the image sampling. A voxel has a finite size and often includes counts from a mixture of tissues with different activity uptakes. So even with a perfect spatial resolution, what is seen is a mixture of the signals coming from different tissues. This is also called the tissue fraction effect and is seen in any imaging modality. Hence, the larger the voxel the greater the tissue fraction effect for a given spatial resolution in the images. [17]

In SPECT the spatially variant collimator-detector response (CDR) degrades the spatial resolution and causes PVEs for small objects. [17] Due to the non-zero acceptance angle, photons coming from some distance away from the collimator surface with a non-parallel incidence angle will be able to pass through the collimator holes. As mentioned, this results in an uncertainty in the positioning of the decay, which increases as a function of the distance. The sensitivity of the system remains the same, but the registered counts will be spread out over a larger detection area. For quantification purposes this will result in a underestimation of the activity concentration quantifi-

cation in small hot regions, since the counts originating from the region are spread out on a larger volume. [10] The effects of this is best handled with a combination of CDR compensation and partial volume corrections, along with choosing an appropriate collimator. [17]

Two other effects that are important for imaging are photon attenuation and scatter contribution. Photon attenuation occurs when photons interact by photoelectric effect or Compton scattering in matter. Interaction probabilities depend on the photon energy, the composition of the material and how much material it is. The attenuation has to be compensated for in SPECT projections, otherwise serious artefacts and false information may occur in the reconstructed images. The scatter contribution within the crystal comes from secondary photons that have Compton-scattered with such small energy loss and in such a direction that they can pass through the collimator holes and be detected in the energy window. The fundamental cause of scatter detection is the poor ability of the NaI system to accurately detect the impacted energy and this also has to be corrected for in the reconstruction of the images. [10]

Another aspect which affects the image and is important to mention is the Poisson noise originating in the projection data. It results from the random nature of the radioactive decay. Each atom of a radionuclide has the same probability to decay, independent of time and the decay of other atoms. Therefore, for a large number of atoms the decay is governed by a Poisson statistics. The number of counts detected by a SPECT is also governed by a Poisson behaviour since all the detection probabilities are independent and random. The variance of the projection data is thus dependent on the number of counts detected. The variance is proportional to the sensitivity of the imaging system, the activity of the source and the acquisition duration. But it is also affected by factors degrading the count rate such as attenuation and scatter. [17]

## 2.5 Monte-Carlo-based simulations

When measurements using clinical cameras can not be proceeded, simulating a SPECT-study is a rather great solution. A very common simulation technique is the Monte-Carlo method. It can be described as a statistical method which uses random numbers as a base to perform a simulation of a given situation. The name was chosen because of the close connection to games based on chance and of the location of a very famous casino in Monte-Carlo. The physical process can in most Monte-Carlo applications be simulated directly. It only requires that the physical process and the system be modeled from known probability density functions (pdf's). If these pdf's can be defined accurately the simulations can be made by random sampling from the pdf's. To obtain reasonable statistical errors, a large number of for example photon histories are necessary to get an accurate estimate of the parameters to be calculated. By using this technique and incorporating the known physics of the scattering process it is possible to simulate scatter events from the object and determine their effect on the final image. [18]

When using Monte-Carlo simulations in nuclear medicine there usually are a series of random events, which together form a single-simulated photon history. The particle must be assigned an initial energy and direction. The particle will then travel a random distance in the assigned

direction until it reaches the next point of interaction. It will then undergo photoelectric absorption, Compton scattering or coherent scattering. If the photon escapes the object it may miss the detector/collimator completely or it may collide front face with it. If the second case occurs then the process may be treated either deterministically or stochastically. When applying variance reduction techniques when simulating random walk processes, simulations of different events will use various techniques. For example, particle birth or absorption. [19]

### 2.5.1 The SIMIND program

SIMIND is a Monte-Carlo-based program which simulates a clinical SPECT scintillation camera and can be easily modified for any measurement or calculation encountered in SPECT. The system consists of two main programs, named CHANGE and SIMIND. With the CHANGE program one can through a menu define the system that will be simulated and write these parameters into an external file. The simulations are then executed with the SIMIND program, which uses the information from the input files provided by CHANGE. It also includes a logical flag system, where the user can turn on or off different features, for example simulation of interaction within the phantom, without the need to change the input files since the flags can be controlled from the command line. [20]

The program SIMIND works in such a way that it is based on uniformly, distributed random numbers for modeling the process of radiation transport. Photons are emitted from a simulated activity distribution in the phantom and are followed step by step towards the scintillation camera. SPECT simulations can be made both for circular and non-circular orbits. Since variance reduction techniques are used, projections are stored as floating-point matrices. [20]

## 2.6 Image reconstruction

Ones the simulations are done and projections are received, they have to be reconstructed into an image. The image reconstruction that is used in this thesis is a iterative one and the task of the reconstruction algorithm is to solve following equation by finding the best estimate of f:

$$P = Af, \tag{8}$$

where p is the measured projection data, A is the system matrix which maps the tracer activity to the projection space. [21]
An initial estimate is assumed for the reconstructed image (solution), and the image is forward projected, simulating and accounting for all possible factors that work together to form the projection data. There are many physical factors that can be handled in the projection step to produce a projection image that is a close match to the acquired projections. The measured and estimated projections are compared in such a way that allows a correction term to be derived. This allows the algorithm to modify the reconstructed slice through an image update and the process is controlled by a cost function or the objective likelihood function as in the maximum likelihood (ML) algorithm. It is very clear that the initial estimate will be far from the solution and therefore the process is continued by repeating the same steps to reach the best estimate of the solution, called

convergence. The system matrix A, from equation 8, holds the information which describes how the projection image is made. It contains the coefficient $a_{ij}$ that denotes the probabilities of detecting a photon emitted from a particular place and detected in a certain bin. In other words the image space is mapped to the projection space by the help of the system matrix that describes the probability of detecting a photon emitted from pixel j and measured in projection bin i such that [21]:

$$p_i = \sum_j a_{ij} f_j. \tag{9}$$

An iterative reconstruction algorithm is based on determining the cost function measuring the agreement between the measured projections and the estimated ones, but also an algorithm for modifying the current activity distribution estimate to optimize the cost function. The most commonly used cost function is as mentioned the maximum likelihood (ML). The goal is to maximize the statistical likelihood of the measured data given the reconstructed image. In emission computed tomography, in the raw projection data, the noise is Poisson distributed, hence the appropriate Poisson likelihood function is maximized. The first and simplest algorithm for maximizing the Poisson likelihood is the expectation maximization (EM), with the resulting algorithm being maximum likelihood expectation maximization (ML-EM). There are a number of limitations with the ML-EM algorithm as it converges to the Poisson ML solution. Its high frequency features in the image converge very slowly, since the image is updated once every iteration. Therefore, to improve the convergence rate the idea of subsets have been introduced to the ML-EM algorithm. Called the ordered subset expectation maximization (OS-EM) algorithm. The idea of this is to divide the projection views into some number of subsets having an equal number of view in each subset and it has a speedup factor of approximately the number of subsets. Meaning that each OS-EM iteration will have the same computation time to one standard EM iteration. The noise properties of OS-EM are not as good as for ML-EM, especially for large number of subsets and very noisy projection data. As a result, for low count data it is desirable to use a small number of subsets. It is also important to note that when using OS-EM or ML-EM the resolution tends to improve and noise tends to increase with increasing number of iterations. [17] Iterative techniques have the advantages of being able to incorporate corrections for image-degrading factors in the system matrix, some of these will be explained later on.

The output given from the reconstructed images are measured in counts. Converting counts to disintegration requires the application of a calibration factor. This factor is based on measured counts of a radioactive source in a experimental set up. [22] Using a parallel hole collimator the calibration factor can be obtained by acquiring a planar image of a thin layer of radioactivity in a thin source placed in air, for example a Petri dish. The count rate is obtained by taking out the total count within a ROI inside the Petri dish subtracted with the total count of ROI‘s outside of the Petri dish, to account for the background activity. Dividing this with the acquisition time and the administered activity, the calibration factor is obtained. [23] An alternative calibration geometry is to use a cylindrical phantom with uniform activity. Then acquisition by SPECT/CT using the same acquisition settings as for the patient studies are performed. Calibrations factors are then obtained as the previous example states.

### 2.6.1 Attenuation correction

Attenuation is one of the biggest factors degrading quantification in SPECT. If attenuation is not compensated for the quantified activity will be underestimated by a factor of 5-20. The size of this effect is greater for low energy photons and for larger and denser parts of the body.[17] A usual method for attenuation correction is the postprocessing method called the Chang method which is applied on the reconstructed images. The method works in such a way that a calculation on an attenuation factor is averaged for all angles and determined for each voxel location within the boundary of the object. It can be described as:

$$AF_{i,j} = \frac{1}{N}\sum_{0} AF_{i,j,0}, \tag{10}$$

where $AF_{i,j,0} = e^{\Sigma^{i,j,\theta}\mu\Delta x}$.
One can also use a method a part of the iterative reconstruction method. Photon attenuation is implemented in the forward projection step before calculating the final projection bin. Since a common feature of all iterative reconstruction methods is the calculated projection obtained by forward projecting a first-guess estimation of an activity distribution into the projection space. By comparing these calculated projections to matched measured projections using some kind of cost function, the want for an improvement of the initial estimated activity distribution can be determined. [21]

In this thesis attenuation maps were retrieved from low dose CT images. The CT-images are in units of Hounsfield (HU) and by transforming them into a map with units of mass attenuation coefficients, $\mu$, for the injected radionuclide a correction for the loss in photons due to attenuation can be made. Scaling the map will take into account the difference between the X-rays from the CT and the emission radionuclide. [17]

### 2.6.2 Scatter correction

The second factor degrading quantification in SPECT is scattered photons. Scatter fractions are in the order of 40 % or more in the thorax and abdomen and 20 % in the brain. The scatter to primary ratio increases almost linearly with source depth, therefore the quantative effects of scatter is larger towards the center of the phantom. [17] There are several ways to correct for scatter and the most commonly used is the Triple-Energy-Window (TEW) which is based on two narrow adjacent-located energy windows around the photopeak window. By taking the average of the acquired images pixel-by-pixel and scale by the ratio between the energy window width of the photopeak window and the scatter window a better scatter estimation will be obtained. Although the problem here is the noise in the scatter data that is mainly a result of the narrow energy windows and scatter images require further processing such as low pass filtering before subtraction. [21]

The scatter correction method used in this thesis is one called ESSE. It does not use energy windows, rather it models the spread based of a CT-image and pre-defined scatter sources, calculated with SIMIND. Basically each voxel is examined as their own radiation source and then convolved with a certain function, thus receiving a description of the spread in water for all directions. It then summarizes all of the results in to a scatter image. [24]

### 2.6.3 Collimator resolution correction and PVE correction

In SPECT, the spatially varying CDR degrades the spatial resolution significantly and creates significant PVE's for small objects. CDR can be compensated for in the iterative reconstruction process. Spatial resolution is often modelled as a Gaussian function, which will mimic the smear out of a point source as a function of distance. To correct for the smear out the source distribution is convolved with the distant dependent Gaussian function. This correction might change the noise texture in the image, where it tends to increase the noise level for the middle frequencies resulting in a blobby texture. The correction might also lead to so called Gibbs-ringing in the images. While the overall volume will be restored, some wave-shaped artefacts can be seen especially close to high gradient regions such as edges. A decrease in the central region of objects might also be seen, which can be falsely interpreted as low uptake. [17] [10] These become more prominent for additional iterations, which might degrade the dosimetry calculations. [25] For organ dosimetry only the total organ activity matters, meaning that summing all of the voxels in an organ averages out the noise and thus drastically reduces the effects of noise and ringing artefact. Partial volume effects thus have the biggest impact for organ dosimetry. Ringing artefacts are most prominent in larger objects, such as the liver. Therefore it is important to optimize the number of iterations used, for them to be as small as possible since a large number of iterations will increase these effects. Although, for small organs with detailed features such as the kidneys, PVEs are the dominant factor degrading the dose results. For them a larger iteration number is needed for optimal validation, so this must be taken in to consideration. [26]

As discussed before, PVE's result from limited spatial resolution of the collimator system and the image sampling in reconstructed SPECT images obtained by either filtered backprojection or iterative reconstruction. Due to this effect, spill-in of counts can be significant when evaluating activity in small regions located near neighboring objects with high activity uptake. Similar, spill-out occurs when quantifying high activity and activity concentrations in small regions. The CDR compensation in the reconstruction does not fix this problem completely and therefore PVC must be applied as well. [21]

The basic idea of all PVC methods is to make the assumption that the activity concentration inside a VOI is uniform and to use this information to compensate for spill in and spill out. This can be corrected by using a calibration method were one uses phantom experiments to estimate recovery coefficients (RC). The RC is defined as the ratio of the measured activity divided by the true activity, [17]

$$RC = \frac{\text{Measured activity in VOI}}{\text{True activity in VOI}}. \tag{11}$$

The RC is a function of the object shape, size, activity relative to the background and the position in the image. Since they are applied to the quantification of small objects, the shape is assumed to be spherical and the background activity is set to zero. Due to this, these methods have limited accuracy. [17]

## 2.7 Image segmentation via thresholding

When segmentation of different structures or organs is needed to be proceeded, for example when creating masks, a way to do so is via thresholding. By finding a pixel value where everything above is in the region of interest and everything below is background, such a pixel value is called a threshold. A simple approach to do so is by using a histogram of pixel values, so that a graph of number of pixels vs. pixel value is obtained. In images where more than one structure is higher in intensity it may be possible to select which structure is the important one. The result of thresholding is an image where all areas above the threshold are set to 1 and all areas below are set to 0. These can be set interactively but there are a few methods for obtaining them automatically. These will not be discussed further, since it is not relevant for this thesis. [27]

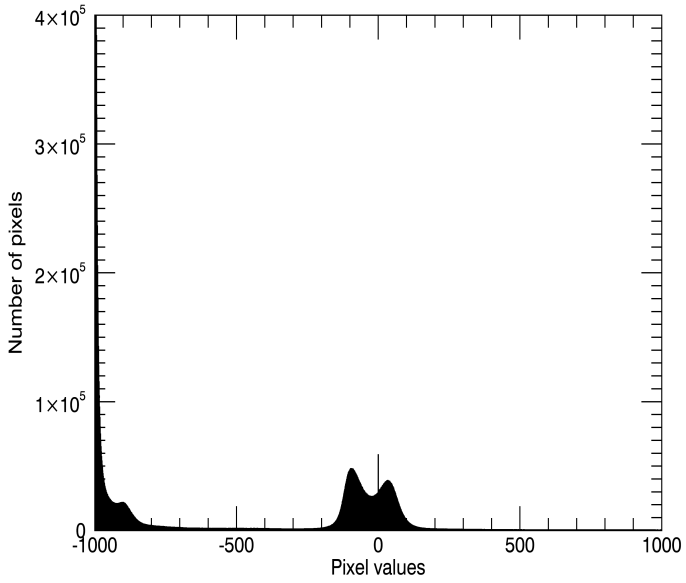


Figure 4: Example of a histogram based of a CT-scan used in this thesis.

# 3 Method

## 3.1 Image data

To begin with it is important to explain what data was given and which was not. During the clinical trial to determine the absorbed dose of $^{225}$Ac based on several imaging procedures, two SPECT/CT measurements and four WB planar images were taken on a total of 13 patients with

three different SPECT-cameras. Data from only 5 of these were chosen for this thesis to be used as our population, since there was not enough time to do what will be explained later for all of them. The patients chosen were 1,2,5,7 and 8 out of the 13.

VOI‘s of the organs of interest for each patient were defined pre-hand, thus segmentation of the organs was not needed to be done during this thesis. The organs segmented were liver, spleen, kidneys, lungs and bone marrow. For patient 1 the lungs were not included. The SPECT/CT‘s and planar images already given were used to decide each patients pharmacokinetic data of $^{111}$In. The CT‘s were also used for the creation of masks or phantoms and as a map to define elliptical VOIs inside the bone marrow and liver, instead of applying RC-corrections.

The acquisition times, injection information and the camera information was also given for each patient. Therefore it was possible to assemble each camera in SIMIND to represent the real ones used on the patients during the trial. Different cameras were used at the different sites and since we wanted to mimic the cameras and patients participating in the study as good as possible, Monte-Carlo simulations were set up with the different cameras. Patients with the same calibration factors, were imaged with the same camera. Calibration factors were calculated for each camera by simulating a Petri-dish with 1 MBq of homogeneously distributed $^{111}$In 10 cm from the collimator. In the following table the calibration factors representing the specific camera used to image each patient and injected activities of $^{111}$In are presented for each patient.

Table 1: Table presenting the calibration factors used for each patient and their corresponding injected activity.

| Information | | |
|---|---|---|
| Patient | Cal. facor [cps/MBq] | Inj. Act. [MBq] |
| 1 | 102.9 | 199.9 |
| 2 | 195.6 | 186.0 |
| 5 | 195.6 | 195.4 |
| 7 | 102.9 | 201.9 |
| 8 | 255.3 | 192.1 |

Another part which was given and calculated beforehand was the effective decay constant of $^{111}$In and $^{225}$Ac. The biological halflife can be derived for $^{111}$In through the given pharmacokinetic data and then it is assumed that they both have the same biological halflife, since they are both attached to a similar monoclonal antibody. In the following table all the decay constants for each organ are presented. These were taken as means from 12 of the patients participating in the clinical trials and standard deviations were calculated between them.

Table 2: The effective decay constants of $^{111}$In and $^{225}$Ac presented for each organ.

| Mean effective decay constants [$h^{-1}$] | | |
|---|---|---|
| Organ | $\lambda_{eff}(^{111}In)$ | $\lambda_{eff}(^{225}Ac)$ |
| Right lung | 0.0156 $\pm$0.0012 | 0.0082 $\pm$0.0012 |
| Left lung | 0.0148 $\pm$0.0017 | 0.0074 $\pm$0.0017 |
| Right kidney | 0.0137 $\pm$0.0024 | 0.0063 $\pm$0.0024 |
| Left kidney | 0.0179 $\pm$0.0033 | 0.0105 $\pm$0.0033 |
| Liver | 0.0138 $\pm$0.0029 | 0.0065 $\pm$0.0029 |
| Spleen | 0.0130 $\pm$0.0012 | 0.0056 $\pm$0.0012 |
| Bone marrow | 0.0140 $\pm$0.0017 | 0.0066 $\pm$0.0017 |

## 3.2 Creation of CT-based phantoms

The first part of the thesis was to create computer phantoms using patient CT-data and files containing VOIs of the organs to be examined. There is a possibility to use already created phantoms such as the XCAT or MCAT phantoms. Although to achieve the most accurate description of our patients the most optimal method was to create phantoms from patient images. Thus the CT images were used for this purpose. To begin with the phantoms were made by creating a mask where the body and skeleton were separated via tresholding and given separate codes for identification. Files with the already segmented organ VOI's were used to merge the segmented organs and the mask together. The skeleton was under the threshold given the same code as the red bone marrow has in the VOI file. Due to difficulties in separating the bone marrow from the vertebrae via segmentation, we chose to treat the whole skeleton as the bone marrow. The SIMIND program will then associate these codes representing each phantom structure with an activity concentration, where both codes and activity concentrations are written in a text-file. Apart from the codes and activity concentrations, the organ names corresponding to each code and their densities are also stated in these text files. The densities of the organs were retrieved from ICRU44 and were set to 1.05 g/cm$^3$ for kidneys, 1.06 g/cm$^3$ for liver, spleen and red bone marrow, 0.26 g/cm$^3$ for the lungs and 1.04 g/cm$^3$ for the remainder. The activity concentrations are given from time activity concentration curves (TACC) which will be explained in the next section.

## 3.3 Time activity concentration curves (TACC)

The activity concentrations were obtained from so called time activity concentration curves (TACC). These curves describe how the activity is distributed in the patient over time. In this case each organ for each patient had one TACC-file, where the curves are derived from known activity concentrations which were previously taken at four different time points by performing planar imaging of the patients. Using the program LundADose curves could be fitted to the activity concentrations. Because it was taken via planar imaging and we are to use SPECT in this thesis, it was necessary to scale the curve as if it was taken by a SPECT. It was also necessary to calibrate the values by using the calibration factors from table 1. The values used to scale between planar imaging values and SPECT were in units of cps/ml and the TAC-files had to be in kBq/ml. Therefore calibration factors were derived by simulating a 10 cm wide and 0.2 mm high Petri-

dish with 1 MBq of $^{111}$In homogeneously distributed in it. The simulations were done for three of the SPECT cameras which were used for the given patient data. For the body or remainder a TAC-file was derived from activity concentrations taken from the two SPECT/CT procedures, where it was derived by calculating the total activity concentration of the body subtracted with the total activity of the organs of interest. Before this method for the body was concluded a few others were tested. The first one was using activity concentrations in the plasma gained from blood samples, although this resulted in over-estimated activity concentrations in the remainder values which exceeded the total injected activity. The second approach was quantifying the total body activity from planar images and then subtracting this with the total activity within the organs of interest. But this resulted in under-estimated activity concentrations in the remainder, where negative values for later p.i. measuring time points were received. Since the total organ activity exceeded the total body one. Thus, using data from the SPECT/CT gave the best conformity. Visual impression of the simulated images with the different methods was also used, where it was concluded that the chosen method was the most optimal.

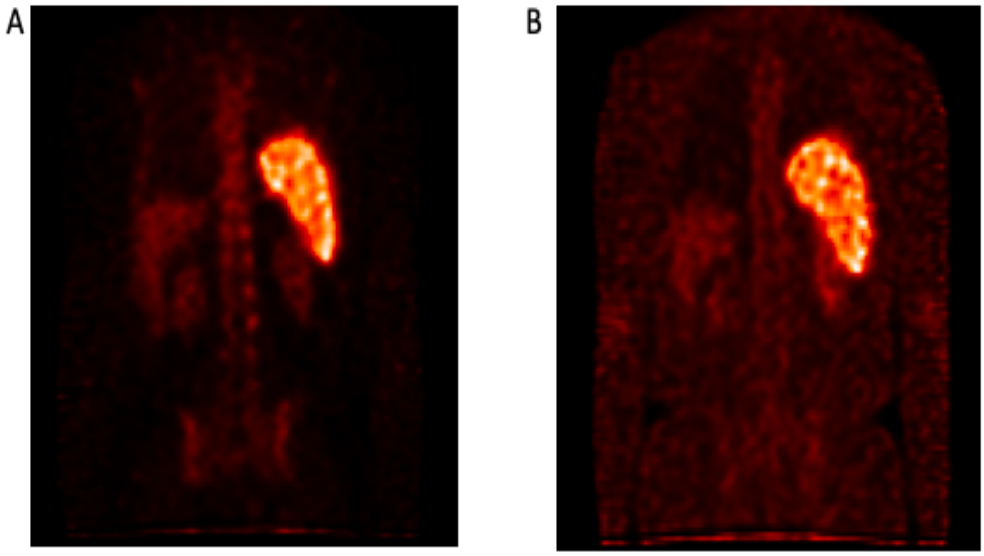


Figure 5: A: Coronal slice of a clinical SPECT-measurement of $^{111}$In. B: Coronal slice of a simulated SPECT-measurement of $^{111}$In representing the same patient and approximately the same time point of measurement as in A.

Figure 5A displays a clinical SPECT-measurement of the activity distribution of $^{111}$In, while figure 5B displays a simulated phantom SPECT-measurement of the same patient at approximately the same time p.i. As shown the background activity within 5B is higher than what it is within the clinical imaging, due to how the TACC's for the remainder were derived.

## 3.4 Recovery coefficient

Due to spill out from the organs we must decide the recovery coefficients (RC). How much of the activity that spills out to other organs and then use this coefficient to calibrate the activities that are

within the region of the organs. The coefficients were calculated by convolution of a point spread function (PSF) with a FWHM of 12 and 10 mm to the spleen, liver, kidneys and bone marrow. The lungs were excluded since recovery coefficients are not applied to the lungs clinically. The RC was given by dividing the filtered image that is inside the region which defines the organs by the total filtered image. Since RC's were calculated for each organ for each patient with a FWHM of 10 and 12 mm means had to be calculated between these and the results were then used as RC's.

Due to the large and inconsistent geometry of the bone marrow/ skeleton a decision was made to not use RC since it will not be a good measurement for spill-out. Instead elliptical VOI's were applied to the vertebrae when quantifying the activity concentration. For this organ three VOI's were placed at different places along the vertebrae and means between these three were then calculated to receive the final activity concentration from the bone marrow. The same procedure was made for the liver except here only one VOI was used in the center of the organ where we assume homogeneously distributed activity, and the RC was excluded from the activity quantification. Since the liver has quite a large volume and relatively small spill-out effect a decision was made that the RC is not necessary. As was mentioned in section 2.6.3 the RCs are applied to small objects where the shape is assumed to be spherical, which we assume for the kidneys and the spleen. The PVE's are also more significant for smaller organs, as mentioned in section 2.6.3, which therefore need to be accounted for with RC. Hence the reason why two separate methods are used.

## 3.5 Simulations and reconstructions

Since SPECT measurements could not be done on clinical cameras, the procedures were simulated in SIMIND were a SPECT-procedure was executed. The camera was set for each patient or phantom to resemble the cameras which took projections of the real patients, during the clinical trials. To begin with each projection was measured for 30 sec in an interval of 120 angles. The energy windows were set for $^{111}$In which has two energy peaks at 171 keV and 245 keV and both are used in this case.

The phantoms were then simulated at 4 different time points, corresponding to the time points used in the image data section, called 4-point test-data. All simulations are reconstructed with 6 iterations, 6 subsets and attenuation, scatter and collimator correction is applied as well as a Poisson distributed noise. The activity concentrations were then quantified from the organ VOI's.

Additional simulations were executed for the new method (1-point dosimetry method). By using equation 14 the optimal sampling time point ($t_{opt}$) could be derived. What is noticed is that different organs will have different $t_{opt}$, due to different effective decay constants. Thus, for this thesis it was decided to examine three different time points. Those are 96 h, 120 h and 144 h, corresponding to 4,5 and 6 days p.i.

## 3.6 Evaluation of TIAC's with current method (4-point method)

The dosimetry calculations for $^{111}$In are based on equation 5 and the activity as a function of time can be described as a sum of exponential functions, see equation 6. The TIAC, $\tilde{C}(r_s)$, was thus given by fitting a biexponential or an exponential with uptake curve in the program LundADose to the four activity concentration points quantified from the reconstructed images. The curves were in the program described with the four parameters C0, $\lambda 1$, C2 and $\lambda 3$. Integration of the curve over a time interval of 0 to $\infty$ for those organs that showed an exponential with uptake behaviour resulted in:

$$\tilde{C}(r_s) = \int_0^\infty -C0 \cdot e^{-\lambda 1 \cdot t} + C2 \cdot e^{-\lambda 3 \cdot t} dt = -\frac{C0}{\lambda 1} + \frac{C2}{\lambda 3}, \tag{12}$$

and for those that showed a biexponential behaviour it was:

$$\tilde{C}(r_s) = \int_0^\infty C0 \cdot e^{\lambda 1 \cdot t} + C2 \cdot e^{-\lambda 3 \cdot t} dt = \frac{C0}{\lambda 1} + \frac{C2}{\lambda 3}. \tag{13}$$

The TIAC's for the 4-point test data were received by first quantifying the activity concentration's for $^{111}$In from the four reconstructed images and then fitting curves to them. The parameters received from this were then put in either equation 12 or 13. To recalculate the TIAC's for $^{225}$Ac either equation 12 or 13 was used where the parameters P1 and P3 were adapted to suit our alpha emitter, since the only thing separating our diagnostic radionuclide from the therapy nuclide is their physical decay constants. Thus $\lambda 1_{Ac}$=$\lambda 1$-$\lambda_{p,In}$+$\lambda_{p,Ac}$ and $\lambda 3_{Ac}$=$\lambda 3$-$\lambda_{p,In}$+$\lambda_{p,Ac}$, where $\lambda_p$ is the physical decay constant of the radionuclides.

Creating the TACC's resulted in parameters describing the true activity distribution within the specific organ over time and by integrating these through equation 12 or 13 the true TIAC's, in our case called reference data, were derived.

## 3.7 Evaluation of TIAC's with new method (1-point method)

As mentioned there is a large interest in simplifying the dosimetric calculations by minimizing the amount of image collections. Since this could mean that more clinics will implement the procedure into their routine. Therefore, simplified methods have been produced by research groups such as Hanscheid et. al. [2] and Madsen et. al. [3]. Although these only suggest a solution for when dosimetry is to be applied to the same radionuclide which was used when imaging. In our case the imaging radionuclide is not what we want to calculate the dosimetry for.

The aim of the 1-point method in this thesis is that by performing one measurement p.i. one could through this single measurement determine the activity distribution over time within the organs of interest. For this thesis, the distribution for the 1-point method was decided to be defined by a mono-exponential function do to reasons of simplification, where the effective decay constant in equation 7, is given as a mean derived between a population of patients participating in the clinical trials. For the approach to be successful, we need to find when the imaging should be proceeded

so when the quantified activity concentration is applied to the mono-exponential equation based on a mean effective decay constant the uncertainties are as minimal as possible for the general person. Therefore, with the help of my supervisors and others we concluded a method that takes account for the relative errors propagating due to the mean effective decay constant and found an equation which will give us $t_{opt}$. The derivation is explained in Appendix, but it resulted in following equation

$$t_{opt} = \frac{1}{\lambda^*_{Ac}}, \tag{14}$$

where $\lambda^*_{Ac}$ is the mean effective decay constant based on a total of 12 patients, presented in table 2. Using equation 14 will give you when the p.i. SPECT-imaging should be proceeded for minimal errors in the TIAC calculations. Since it is dependent on the mean effective decay constant of $^{225}$Ac and is different for each organ $t_{opt}$ should variate between the organs. Therefore, $t_{opt}$ might have to be chosen depending on which organ is the main objective. Or one could say, for which organ it is more important to have minimal errors. By applying the effective decay constants for $^{225}$Ac from table 2 to equation 14 we get following $t_{opt}$ for the different organs: 154 h for the liver, 178 h for the spleen, 127 h for the kidneys, 152 h for the bone marrow and 128 h for the lungs. Although for the kidneys and lungs they were derived as means between the left and right.

The time integrated activity concentration per injected activity (IA) for $^{225}$Ac using a mono-exponential function is defined as

$$\tilde{C} = \frac{C_{Ac}(0)}{\lambda_{e,Ac}} = \frac{K \cdot C_{In}(0)}{\lambda_{e,Ac}}, \tag{15}$$

where K=$\frac{1}{A_{inj,In}}$. Equation 15 can be expressed in terms of quantified activity concentration of $^{111}$In at a given time point, t, thus giving us:

$$\tilde{C}^* = \frac{K \cdot C_{In}(t) e^{\lambda^*_{In} t}}{\lambda^*_{e,Ac}}. \tag{16}$$

The optimal time-point, given from equation 14, is then applied to equation 16, along with the quantified activity concentration of $^{111}$In from the reconstructed SPECT-image.

## 3.8 Procedure

Since the method consist of many steps these will be thoroughly explained in this section, with flowcharts and explaining text. As mentioned CT-based phantoms and TACC's were created and used as input in SIMIND. To be able to test the 1-point method for calculating the dosimetry the one used today was first executed. Thus, four simulations and reconstructions at four different time-points p.i. for all five phantoms were executed. The time points correspond to those used when planar images were taken of the patients during the beginning of the study. After that the activity concentrations were quantified for the kidneys, lungs, liver, spleen and bone marrow in all reconstructions. Recovery coefficients were then applied to the activity concentrations and new curves were fitted to the values so TIACs/IA could be calculated, called it 4-point test-data. These were then used to calculate the TIAC's/IA for $^{225}$Ac.

These were compared to reference-data, activity concentrations taken directly from the TACC's and TIAC's calculated using the parameters which describe our TACC's. The relative deviations between the test- and reference-data were calculated for the activity concentrations and TIAC's, to examine the uncertainties which propagate from the activity concentrations quantification into the dosimetry calculations, but also to see how big the uncertainties are within the 4-point method. Following equation describes how the relative deviations were calculated:

$$\text{Rel. Deviation} = \frac{\hat{C}_{test} - \hat{C}_{ref}}{\hat{C}_{ref}} \cdot 100 \tag{17}$$

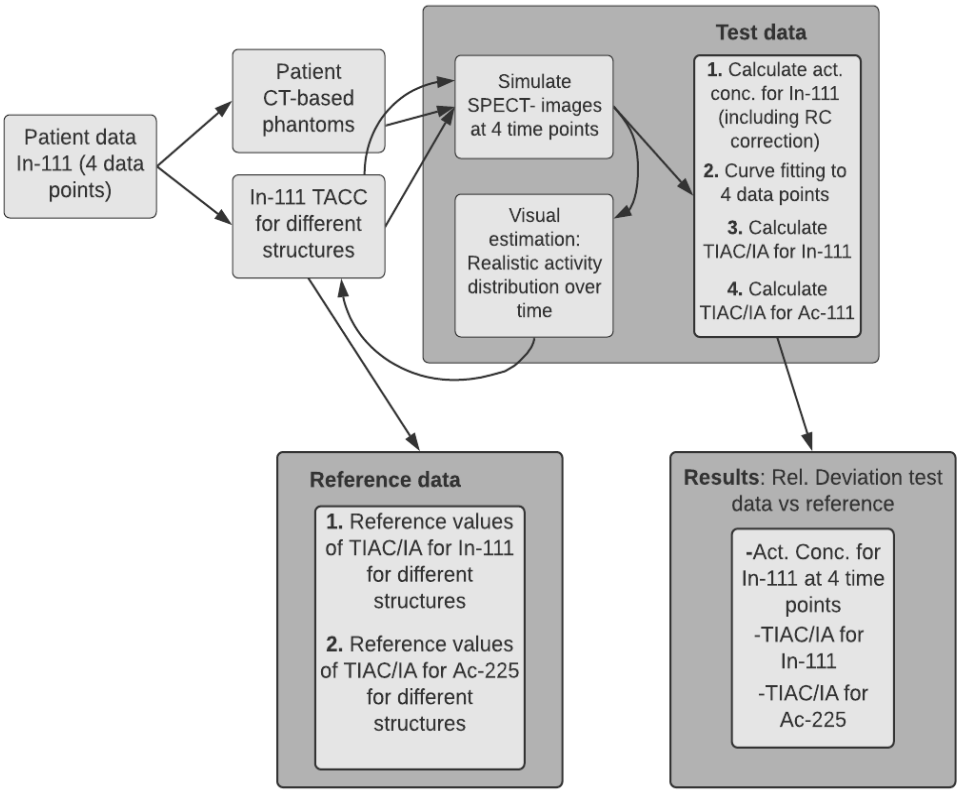


Figure 6: Flowchart explaining what was done during the first part of the thesis.

For the second part the TIAC's with only one SPECT procedure were calculated. Here the TIAC's for three different time points are examined to see how much the absorbed dose will differentiate between when that one SPECT is completed. What is noticed is that the optimal time in equation 14 will variate depending on what organ one is interested in examining, since the effective half-life differentiates between organs due to the biological half-lives. Therefore, three different optimal times are looked at to see how the single measurement absorbed doses will differ between them. The time points chosen were 4, 5 and 6 days p.i. These were chosen since our main objective are the kidneys and bone marrow, and to give examples which are suitable for clinic use.

Once the TIACs using only one SPECT-procedure are calculated, called them 1-point test data, relative deviations between them and 4-point method test data, reference-data and TIAC's given by the 1-point method where activity concentrations are taken directly from the TACC's are calculated. Equation 16 will give us TIAC's for $^{225}$Ac directly and no recalculations needs to be done. The following image shows a flowchart of how the second part of the method was proceeded.

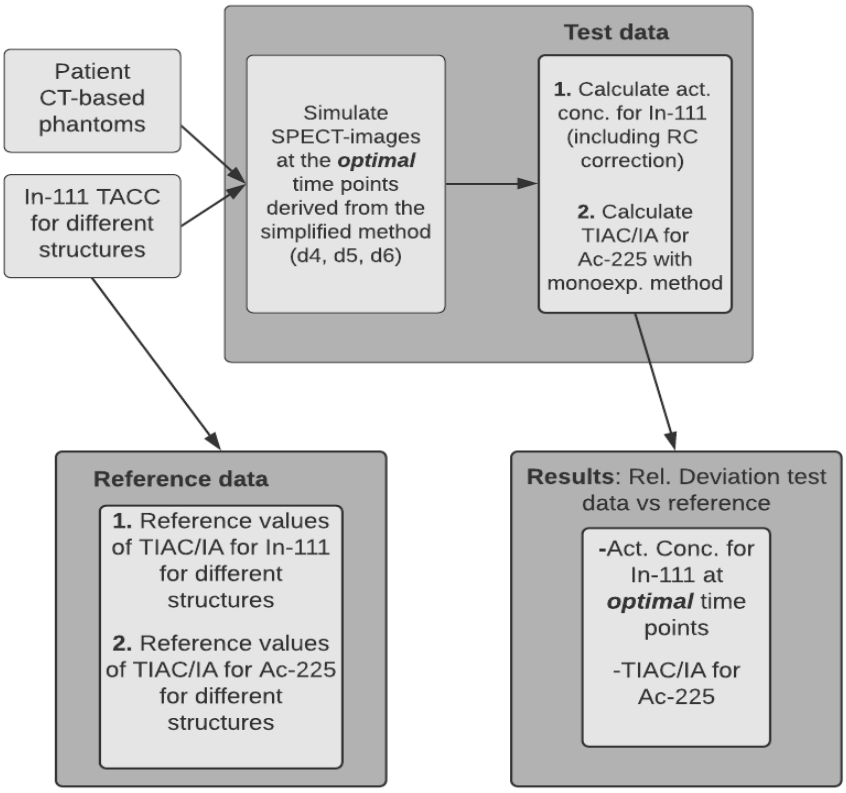


Figure 7: Flowchart explaining what was done during the second part of the thesis.

# 4 Results

## 4.1 CT-based phantoms

The CT-based phantoms where a big part of this thesis and since much work was put into creating as realistic phantoms as possible one slice from two different phantoms and their corresponding CT-slice are presented in this section. Each organ had a certain code given to them, which was the same for every phantom. It was thus easy to distinguish them from each other and possible for SIMIND to simulate by placing the correct activity concentration within the correct organ.

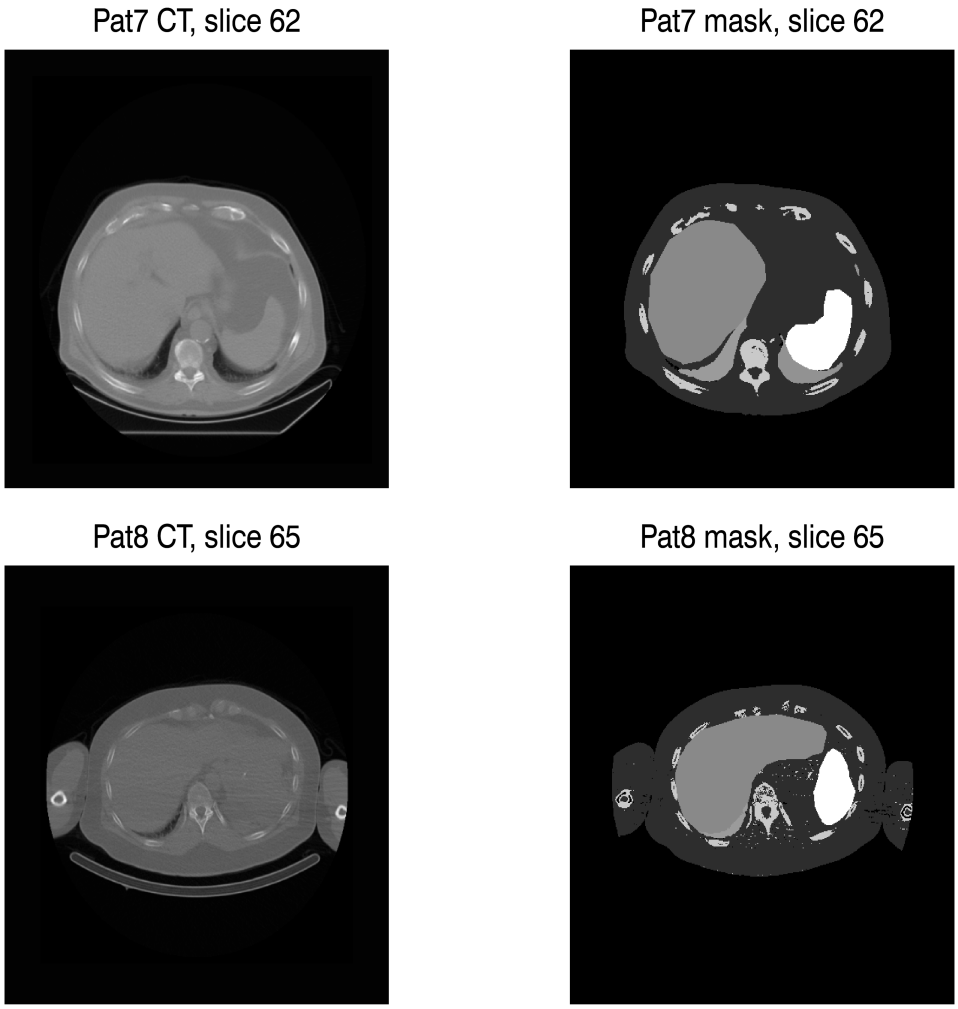


Figure 8: Masks and CT‘s for patient 7 and 8.

In figure 8 the organs shown for patient 7 (pat7) are liver, spleen, skeleton (bone-marrow), remainder and a small part of the lungs. The corresponding CT-scan is also displayed in figure 8 to show where the mask originates from and to visually see how well they correspond.
The organs portrayed for patient 8 (pat8) in figure 8 are liver, spleen, skeleton (bone-marrow) and remainder, which are segmented from the corresponding CT-scan portrayed next to the mask.

## 4.2 TACC

In the following section the TACCs for each organ and each patient in the population are presented. The lungs and the kidneys are here separated as left and right to show the difference in pharmacokinetics, but also since the separate files were used as input in SIMIND. Although for the calculations the left and right are treated as one organ and for each calculation means where taken between them.

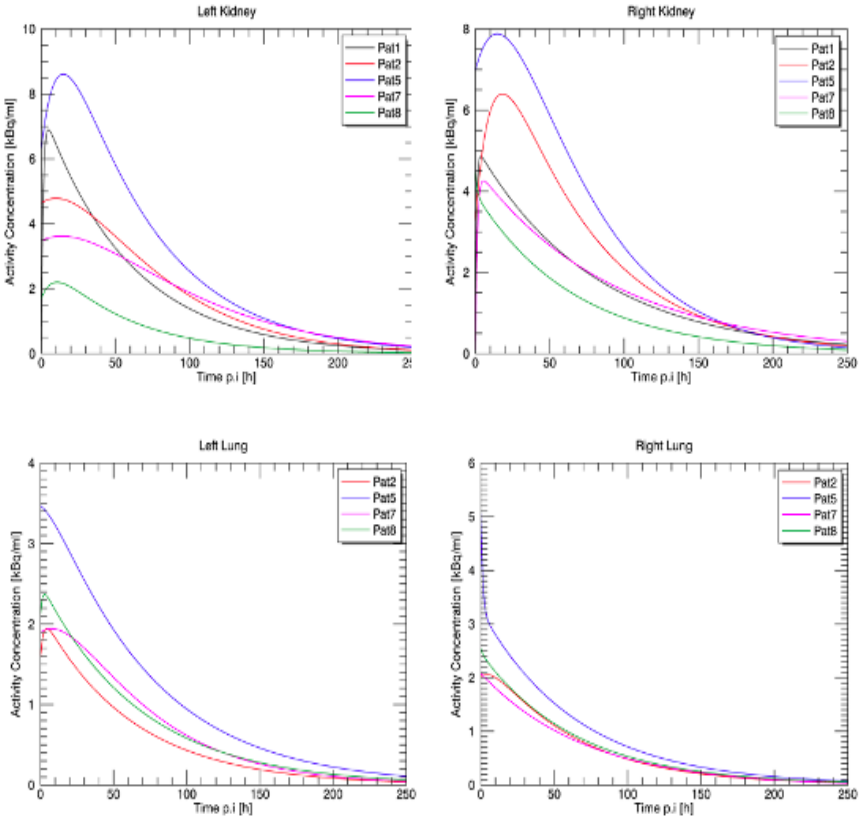


Figure 9: TACC's for the lungs and kidneys.

The above figure shows the kinetics of the lungs and the kidneys for all patients used in this thesis. These show clearly that the kinetics are different between the left and right organ and that they do not behave the same when it comes to uptake and secretion. Although as mentioned the left and right are treated as one whole organ, since that is how it is done clinically. They also portray how the same organ for different people will take up and secrete the same radiopharmaceutical differently.

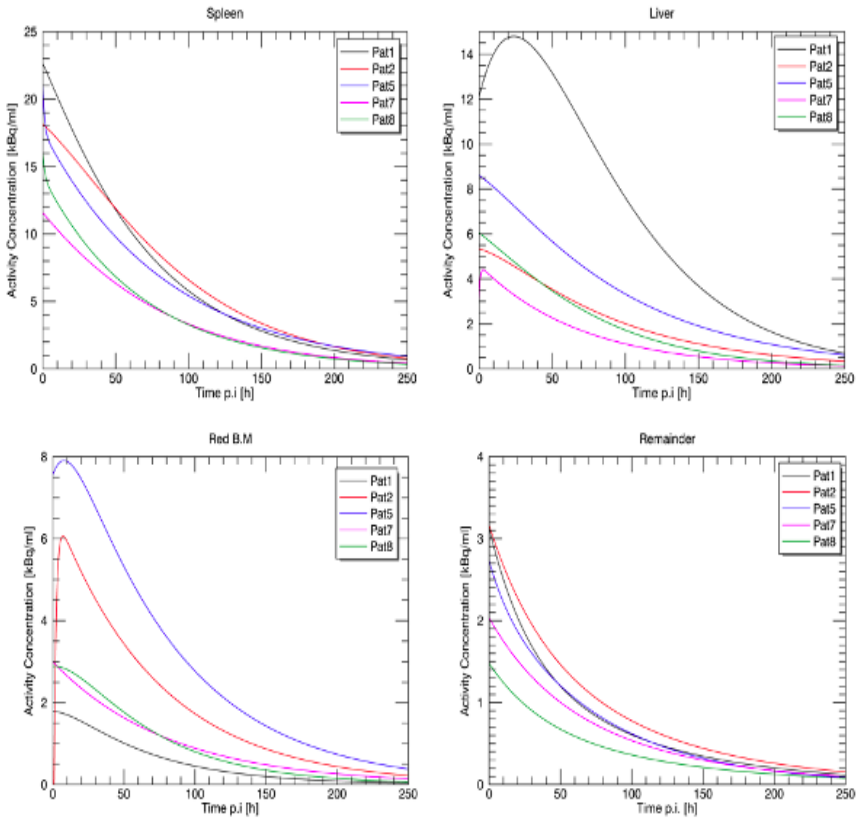


Figure 10: TACC‘s for the liver, spleen, bone marrow and remainder.

The above figure displays the TACC‘s for the remaining organs spleen, liver, bone marrow and remainder. Here as well it is clearly shown how the pharmacokinetics variate between different people. For example if one looks at the liver where patient 1 (pat1) has a higher uptake of the injected activity but also behaves very differently in the secretion.

## 4.3 Recovery Coefficients

In the following table the recovery coefficients for the kidneys, liver, bone marrow and spleen are presented. These were calculated to correct for the spill-out effect, by convolution of a PSF with a FWHM of 10 and 12 mm over the organs of interest. The RC’s were calculated to be 0.78 for the kidneys, 0.86 for the spleen, 0.91 for the liver and 0.55 for the bone marrow. Even though RC’s were calculated for the bone marrow and liver, these were not used on the quantified activity concentrations. Due to the livers large volume and relatively small spill-out effect and because of the bone marrows large and inconsistent geometry, the RC is not a good measurement for spill-out since it is suited for small and spherical objects. Instead elliptical VOI‘s were created and placed in the center of the organs to read out the activity concentrations. For the bone marrow three different VOI‘s along the vertebrae were used and then a mean activity concentration was derived. While for the liver only one VOI was used and placed in the middle of the organ were it was assumed that the activity distribution is homogeneous. Hence the two different methods to

determine the activity concentration.

Table 3: Method used to correct for spill out.

| Organ | RC [1] |
|---|---|
| Kidneys | 0.78 |
| Liver | 1 elliptical VOI |
| Bone Marrow | 3 elliptical VOIs |
| Spleen | 0.86 |

## 4.4 Part 1- reference data and test data with 4-point method

In the first part the uncertainties in the 4-point method are examined to see how big uncertainties we have in the quantification's but also the calculations. In table 4 the mean relative deviations, and their standard deviations between the five patient phantoms, of the activity concentrations between test data and reference data for $^{111}$In are presented. While in table 5 mean relative deviations in TIACs for $^{111}$In and $^{225}$Ac between 4- point test-and reference-data are presented, along with their standard deviations.

For the lungs and kidneys activity concentrations and TIAC's were derived for the left and right organs separately and then means between them were calculated.

Table 4: Mean relative deviation between activity concentration test data and reference data for $^{111}$In.

| Rel. Deviation [%] | | | | | |
|---|---|---|---|---|---|
| Time point | Spleen | Kidneys | Liver | Lungs | Bone Marrow |
| 1 | 3.5 ±10.1 | 19.7±14.3 | 3.0±8.9 | 2.1±14.4 | -2.1±23.9 |
| 2 | 1.6 ±12.8 | 9.6±12.7 | 3.9±13.8 | 2.7±16.9 | -4.8±20.9 |
| 3 | 1.9 ±10.4 | 12.8±13.9 | 2.7±16.6 | 3.8±17.6 | -6.5±23.8 |
| 4 | 2.3 ±11.8 | 26.3±16.5 | -1.7±16.6 | 15.9±29.3 | -8.1±15.5 |

Table 5: Mean relative deviation of TIAC between test data and reference data both derived with the 4-point method.

| Rel. Deviation [%] | | | | | |
|---|---|---|---|---|---|
| Radionuclide | Spleen | Kidneys | Liver | Lungs | Bone Marrow |
| $^{111}$In | 2.2±11.1 | 22.2±11.0 | 1.6±13.1 | 6.3±17.9 | -4.7±21.6 |
| $^{225}$Ac | 2.4±11.2 | 25.4±7.4 | -1.4±15.6 | 11.2±21.1 | -6.9±21.7 |

## 4.5 Part 2- reference data and test data with 1-point method

For the second part of the calculations the uncertainties in the 1-point method are examined. In this section the mean relative deviation between the TIAC's calculated with equation 16, reference data, test data and TACC data are presented in tables. The relative deviations are taken as means between the population and are presented with their corresponding standard deviations.

Table 6: Mean relative deviation between TIAC given with the 1-point method where act. conc. are taken directly from the TACC's and reference data.

| Rel. Deviation [%] | | | | | |
|---|---|---|---|---|---|
| Time p.i [h] | Spleen | Kidneys | Liver | Lungs | Bone Marrow |
| 96 | 8.9 ±12.2 | 7.5 ±14.2 | 3.6 ±22.4 | 1.3 ±2.5 | 2.6 ±11.8 |
| 120 | 7.7 ±10.7 | 7.9 ±9.1 | 4.8 ±19.7 | 0.5 ±0.6 | -0.3 ±7.9 |
| 144 | 6.0 ±9.1 | 8.0 ±6.3 | 5.1 ±15.8 | -0.6 ±1.8 | -0.1 ±2.9 |

Table 7: Mean relative deviation between activity concentrations from 1-point test data and act. conc. taken directly from the TACC's at the given time points.

| Rel. Deviation [%] | | | | | |
|---|---|---|---|---|---|
| Time p.i [h] | Spleen | Kidneys | Liver | Lungs | Bone Marrow |
| 96 | 2.7 ±11.7 | 19.9 ±10.9 | 7.8 ±13.3 | 9.1 ±18.2 | 2.4±35.1 |
| 120 | 2.0 ±10.9 | 21.1 ±8.9 | -0.2 ±10.1 | 11.7 ±19.8 | -6.6 ±22.9 |
| 144 | 1.6 ±11.1 | 22.1±8.4 | -4.6 ±9.7 | 12.9 ±20.5 | -3.5±19.1 |

Table 8: Mean relative deviation of TIAC between 1-point test data and reference data.

| Rel. Deviation [%] | | | | | |
|---|---|---|---|---|---|
| Time p.i. [h] | Spleen | Kidneys | Liver | Lungs | Bone Marrow |
| 96 | 11.7 ±17.4 | 26.6 ±10.7 | 10.5 ±20.2 | 10.8 ±21.3 | 5.8 ±43.4 |
| 120 | 9.8 ±16.0 | 29.3 ±7.1 | 4.6 ±21.8 | 12.2 ±21.1 | -5.6 ±29.4 |
| 144 | 7.7 ±15.8 | 31.4 ±10.2 | -0.01 ±16.1 | 12.0 ±19.7 | -3.8 ±17.5 |

Table 9: Mean relative deviation of TIAC between 1-point test data and 4-point test data.

| Rel. Deviation [%] | | | | | |
|---|---|---|---|---|---|
| Time p.i. [h] | Spleen | Kidneys | Liver | Lungs | Bone Marrow |
| 96 | 9.1 ±11.9 | 2.7 ±11.3 | 13.4 ±22.5 | -0.2 ±5.3 | 11.4 ±20.3 |
| 120 | 7.2 ±9.9 | 4.3 ±6.9 | 7.5 ±23.6 | 1.2 ±5.4 | 2.1 ±26.8 |
| 144 | 5.1 ±8.7 | 5.3 ±3.9 | 2.1 ±11.9 | 1.2 ±4.0 | 5.4 ±18.5 |

# 5 Discussion

## 5.1 CT-based phantoms and TACC

For the human based phantoms or masks, as mentioned the goal was to make them as realistic as possible. Therefore, we decided to use the CT's of the patients and the already segmented organs. Using the thresholding technique and then merging the organ VOI's to the masks was over all a rather successful approach. Although it resulted in many other organs and tissues being excluded and only marked as remainder. By excluding organs it might result in an overestimation or underestimation of the activity concentration in some parts of the remainder since these parts are not studied. Thus, what could have been made better and more realistic is the segmentation of the phantoms by including more organs. Which might have resulted in more accurate activity

concentrations in the background/remainder. This would further make it possible to decide the exact spill-in and spill-out of the different organs and therefore receive a more accurate activity concentration quantification over all.

If more time was given another part which would be interesting to solve is the merging of the bone marrow. Due to difficulties in segmenting and thresholding the bone marrow from the skeleton, a decision was made that the bone marrow should be placed in the whole skeleton in the phantoms, instead of only in L2-L4 of the vertebrae as intended during the clinical trials.

## 5.2 Recovery Coefficient

The RC‘s where derived according to the method explained in section 2.6.3 and 4.3. This means that when the convolution was proceeded it is assumed that the background is cold, meaning it has no activity within it. Therefore they only take into account for the spill-out which might occur and no spill-in. This might affect the results and lead to overestimated values which are not accounted for. Even though it is hard to correct for spill-in, it should be analyzed and as explained in the section above, if the phantoms were more realistic that might have been possible.

Inconsistent geometry led to highly overestimated values in activity concentration quantification of the skeleton/bone marrow when the RC was used. Therefore, elliptical VOI’s were used instead. For future work, it would be interesting to see the effect on the results when using different types of VOI‘s placed along the vertebrae. For example, examining how the size and shape affect the quantification and then finding which is optimal to use. If we then could solve the segmentation issue of the bone marrow along with optimizing the quantification, the results could probably be even better. For the liver there is a possibility that ringing artefacts have led to a higher activity concentration at the edges of the organs compared to the centre, as discussed in section 2.6.3. By then applying a VOI in the centre for the quantification this might result in some data being lost. Although no ringing artefacts could be seen, therefore this approach was still deemed to be valid. For the kidneys and the spleen, the PVE’s were substantial enough that VOI’s would not have been a good approach due to significant data could be lost. It would also be difficult to apply decent VOIs without any impact from the surrounding tissues. Therefore two different methods were decided to be used, but if more time was given this could also be something to examine.

## 5.3 Part 1- reference data and test data with 4-point method

It was suitable to evaluate the uncertainties in the 4-point method to know whether or not the 1-point method is successful enough. From table 4 one sees that there is a deviation between the reconstructed activity concentrations and the true ones, 4-point test and reference data. For most of the organs the reconstructed values are overestimated, especially the kidneys. The kidneys will be overestimated probably due to their low activity concentration, their small sizes and the rather high activity concentration of the remainder. Looking at figure 9 and 10 the remainder and the kidneys have approximately the same amount of activity concentration. Since spill-in from the remainder is not accounted for, combined with the kidneys small size might result in this truly

affecting the quantification.

The bone marrow is underestimated probably due to its inconsistent geometry, the difficulties in applying decent VOIs within the organ or deriving RC corrections. The results in table 4 over all indicate that simulating a SPECT-measurement and reconstruction of the projections with all corrections will mostly result in an overestimation of quantification for a population. Thus resulting in the mean doses being overestimated compared to reference data, but as the standard deviations imply for individual patients they can vary substantially.

Therefore analyzing the results in table 5 the mean deviations are promising, but for each individual patient it might deviate a great deal. The kidneys have a higher uncertainty probably do to very low activity uptake, as explained above. The same holds for the lungs which seem to have rather okay mean values, but looking at their standard deviations they deviate a great deal between individual patients. Analyzing the results one could say that there are two major errors propagating into the dose calculations. The first is as mentioned due to the SPECT-study and reconstruction where we can not receive a 100 % accurate conversion. The second could be the uncertainty in the curve fitting to the quantified activity concentration values, which needs to be made to receive the TIAC's. The curves are not always a 100 % fit to the values which can affect the end result of the TIAC.

## 5.4 Part 2- reference data and test data with 1-point method

The biggest question of this thesis was if it is possible to minimize p.i. SPECT measurements and still receive valid dosimetry results. In table 6 where the relative deviations between the TIAC's given with 1-point method where activity concentrations are given from the TACC's and reference data are presented, the relative deviations represent the uncertainty in the 1-point method derivation for each p.i. measurement. For the population as a whole the uncertainties show promising results, meaning that the mean errors within the 1-point method lie around -1 % to 9 %. The uncertainty in this method should mostly come from the mean effective decay constant, which has an uncertainty in the biological decay constant and will thus propagate into the relative deviations of the 1-point dosimetry calculations. The mean effective decay constant, presented in table 2, is based on pharmacokinetic data taken from 12 patients during the clinical trial. If 1-point dosimetry is to be implemented clinically an optimization according to each individual patient can't be made and already given values of the decay constants, $\lambda^*$, have to be used. In our case it is based of a population of 12 patients, which of course isn't ideal since the greater the population the more precisely the constants can be decided. Thus, the end results will not be affected as much on existing extremities within the effective decay constant.

According to equation 14, $t_{opt}$ for the liver lies around 150 h p.i. It is therefore hard to explain why we receive a smaller mean relative deviation at 96 hours p.i. than for 144 hours p.i. It seems as if for the individual patient the results will be better for later p.i. measurements than earlier since the standard deviations are the smallest for 144 hours. Before means were calculated, what

is noted for individual phantoms is that the relative deviation gets better for 144 h p.i. Due to large variations in the TIAC's between phantoms, and two phantoms resulting in negative relative deviations for all sampling time points, the method will appear to be optimal at 96 h p.i. when means are taken between them. The spleen on the other hand has a very clear behaviour where the uncertainties are the smallest for later p.i. measurements, which follows the theory discussed in section 3.7. The same could be said for the bone marrow, even though there isn't a large difference between the mean relative deviations for 120 and 144 h p.i. It is also hard to say if there is any optimal calculation time for the kidneys since the mean values are practically the same but the standard deviations become better for later p.i. calculations. The same holds for the lungs, although one could say that the optimal calculation time for them is 120 h p.i. since the relative deviation and the standard deviation are the lowest at this point. This was also expected from the theory. All in all, the results from table 6 indicate that the 1-point method compared to reference data will for most of the organs have reasonable deviations. What can be said, if possible, for future work it would seem as a good idea to add more phantoms to the population as well as more patient data to the calculation of the mean effective decay constant. This will probably lead to better and more accurate results, since they will not depend on extremities as much.

Going to table 7 and analyzing the results of relative deviations between activity concentrations from 1-point test data and activity concentrations taken directly from the TACC's at the given time points, we have calculated the uncertainty in the quantification's of the activity concentrations. Here, as in table 4, the kidneys have a larger uncertainty than the rest of the organs. Looking at figure 9 we see that the kidneys have a quite low activity concentration at the studied time points, which will bring difficulties in imaging them. They also have approximately the same concentration as the remainder, and as we correct for spill-out we do not correct for spill-in from the remainder. Which, as mentioned in section 5.3, might be the reason for the large uncertainties in the quantification. The same holds for the lungs, although they are not as affected by the remainder as the kidneys and thus the spill-in is not as significant. They are also not corrected for spill-out since it is not proceeded clinically. For future work what would be interesting to examine is the effect of longer acquisition time, to see if the results get better the more data the SPECT collects or if it stays approximately the same.

Looking at table 8, where the relative deviation between the 1-point method test data and reference data is presented and comparing it to table 5 where the 4-point method test data is compared to reference data, the 1-point method does not deviate awfully much from the true values. These results are probably the ones which are of most value, since the 1-point test data are those expected to be received if the method was proceeded clinically. Here the spleen, liver and bone marrow result in the smallest relative deviations for later p.i. measurements. All three organs have an $t_{opt}$ in the region of 150 hours p.i. or later. Looking at the lungs for example there is not a huge difference in the deviations between the different sampling times, just as there was not a large difference in table 6. Comparing them with the results in table 5, the 1-point dosimetry works just as well as the 4-point method does for the lungs. When it comes to the kidneys the large uncertainty in the quantification's are clearly shown in the results presented in table 8. The TIAC's will be overestimated compared with the true values (reference data), but the results are

not better when the calculations are made with the 4-point method. The bone marrow on the other hand seems to be underestimated, even with the 4-point method calculations. What can be said is that these results show that for the bone marrow, as for the liver, the 1-point dosimetry calculations at 144 hours p.i. result in better relative- and standard-deviations than when TIAC's are calculated with the 4-point method. For the kidneys on the other hand it is harder to say which method is the optimal one. Comparing the results for the kidneys received with the 1-point method to the 4-point method, the later resulted in smaller deviations at around 25.4 $\pm$7.4 % and for the 1-point method at 96 h p.i. 26.6 $\pm$10.7 %. Even though the deviations at 96 h p.i. for the 1-point method were not far off, if the kidneys are the only organs of interest it is hard to say which method is better. If we then include the bone marrow as well, the other main objective, with their optimal results at 144 h p.i. deciding which time point one should use is difficult. Especially since the standard deviation for the bone marrow at 96 h p.i. is so significant.

Finally, analyzing the results in table 9, where the relative deviations of the test data between TIAC's derived with the 1-point method and 4-point method are compared. This on the other hand shows that the 1-point method will overestimate the doses if one compares them with measurements and calculations done according to the 4-point method. The results are promising with deviations around 5 % for later p.i. measurements. With such small deviations from the 4-point test data and from reference data one could say that the 1-point method is as good as the old one.

# 6 Conclusion

Through careful discussion one can conclude that the 1-point method is quite successful. When compared to the true data, the errors calculated with the 1-point dosimetry method are in the same region compared with the errors calculated with the 4-point dosimetry method. It is difficult to know how well this data represents true patients, since all our data is based on simulated SPECT procedures. If all the measurements where proceeded with real patients on clinical cameras the results might have been completely different, but that was not possible. Although, in this study where we compare simulated data against what we defined as our reference data we receive similar results between the 1-point method and 4-point method.

For organs such as the spleen, liver and bone marrow the results show that the single measurement should be proceeded at around 144 hour p.i. or later as their derived optimal sampling time points predict. While the results showed that for the kidneys, which are the main objectives, an optimal measurement is around 96 h p.i. even though their derived optimal sampling time is around 120 h p.i. It is hard to say why this is the case, throughout the discussion it has been mentioned that spill-in from the remainder into the kidneys might result in a significant deviation from the true values. Therefore, for future work it would be a good idea to try and solve this issue which is not approached in this thesis. Either by finding appropriate spill-in corrections or by determining the activity concentration within the remainder more accurately. Comparing the results for the kidneys received with the 1-point method to the 4-point method, the later resulted in smaller deviations. Even though the deviations at 96 h p.i. for the 1-point method were not far off. There-

fore if the focus only lies upon the kidneys it is hard to say which method is better. If we then include the bone marrow as well, the other main objective, with their optimal results at 144 h p.i. deciding which time point one should use is difficult. Therefore, including more patient data to the results would be a good idea to receive more accurate deviations and specifically smaller standard deviations.

All in all, considering the amount of resources and time that could be saved with the 1-point method, the results presented in this thesis indicate that it is possible to determine absorbed doses based on a single SPECT-measurement. For some organs the 1-point method shows better results for later time points, while the results at 96 h p.i. with the 1-point method are about the same as with the 4-point method for the kidneys.

# 7 Acknowledgments

First of all I would like to express my gratitude to my supervisors Michael Ljungberg and Katarina Sjögreen Gleisner for giving me this opportunity to join them on this project and thank them for all their guidance and help during this semester. I would also like to thank Johan Gustafsson for his work on the optimal time point derivation, without him that would not have gone as smooth as it did.

I would also like to thank my classmates, especially those whom I have shared office space with during this semester. Without the endless coffee breaks and interesting topics of discussion, this semester would not have been half as fun as it was.
Finally, I would like to thank my family and especially my fiancé Haris Kapidzic for always supporting and believing in me, not only in these past months but throughout my studies.

# References


[1] Jackson PA, Hofman MS, Hicks RJ, Scalzo M, Violet J. Radiation Dosimetry in 177Lu-PSMA-617 Therapy Using a Single Posttreatment SPECT/CT Scan: A Novel Methodology to Generate Time-and Tissue-Specific Dose Factors. Journal of Nuclear Medicine. 2020;61(7):1030–1036.

[2] Hänscheid H, Lapa C, Buck AK, Lassmann M, Werner RA. Dose mapping after endoradiotherapy with 177Lu-DOTATATE/DOTATOC by a single measurement after 4 days. Journal of Nuclear Medicine. 2018;59(1):75–81.

[3] Madsen MT, Menda Y, O'Dorisio TM, O'Dorisio MS. Single time point dose estimate for exponential clearance. Medical physics. 2018;45(5):2318–2324.

[4] A Scheinberg D, R McDevitt M. Actinium-225 in targeted alpha-particle therapeutic applications. Current radiopharmaceuticals. 2011;4(4):306–320.

[5] Fusion Pharmaceuticals Inc., The Fusion Pipeline; 2020. Accessed: 2020-01-12. `https://fusionpharma.com/fusion-pipeline/`.

[6] Miederer M, Scheinberg DA, McDevitt MR. Realizing the potential of the Actinium-225 radionuclide generator in targeted alpha particle therapy applications. Advanced drug delivery reviews. 2008;60(12):1371–1382.

[7] Wu TJ, Chiu HY, Yu J, Cautela MP, Sarmento B, das Neves J, et al. Nanotechnologies for early diagnosis, in situ disease monitoring, and prevention. In: Nanotechnologies in preventive and regenerative medicine. Elsevier; 2018. p. 1–92.

[8] Chechev VP. Laboratorie National Henri Becquerel(LNHB), $^{111}$In; 2006. Accessed: 2020-01-12. `http://www.lnhb.fr/nuclides/In-111_tables.pdf`.

[9] Khalil M. Basic sciences of nuclear medicine. Springer Science & Business Media; 2010. Pages 35-36.

[10] Ljungberg M, Gleisner KS. Hybrid imaging for patient-specific dosimetry in radionuclide therapy. Diagnostics. 2015;5(3):296–317.

[11] Hindorf C. Nuclear medicine physics: a handbook for teachers and students. Iaea; 2014. Chapter 18.

[12] Bailey DL, Humm J. Nuclear medicine physics: a handbook for teachers and students. Iaea; 2014.

[13] Ljungberg M. Basic sciences of nuclear medicine. Springer Science & Business Media; 2010. Pages 285-308.

[14] Khalil M. Basic sciences of nuclear medicine. Springer Science & Business Media; 2010. Pages 155-170.

[15] Lawson RS. Practical SPECT/CT in nuclear medicine. Springer; 2013. Pages 47-75.

[16] Cherry SR, Sorenson JA, Phelps ME. chapter 14 - The Gamma Camera: Performance Characteristics. In: Cherry SR, Sorenson JA, Phelps ME, editors. Physics in Nuclear Medicine (Fourth Edition). fourth edition ed. Philadelphia: W.B. Saunders; 2012. p. 209 – 231. Available from: `http://www.sciencedirect.com/science/article/pii/B9781416051985000149`.

[17] Buvat I, Frey E, Green A, Ljungberg M. Quantitative nuclear medicine imaging: concepts, requirements and methods. Human Health Reports. 2014;9.

[18] Ljungberg M. Monte Carlo Calculation in Nuclear Medicine: Applications in Diagnostic Imaging - Second Edition. Francis Taylor; 2012. Chapter 1.

[19] Haynor DR, Harrison RL. Monte Carlo Calculation in Nuclear Medicine: Applications in Diagnostic Imaging - Second Edition. Francis Taylor; 2012. Chapter 2.

[20] Ljungberg M. Monte Carlo Calculation in Nuclear Medicine: Applications in Diagnostic Imaging - Second Edition. Francis Taylor; 2012. Chapter 7.

[21] Khalil M. Basic sciences of nuclear medicine. Springer Science & Business Media; 2010. Pages 259-283.

[22] Khalil M. Basic sciences of nuclear medicine. Springer Science & Business Media; 2010. Pages 139-140.

[23] Ljungberg M, Gleisner KS. 3-D Image-Based Dosimetry in Radionuclide Therapy. IEEE Transactions on Radiation and Plasma Medical Sciences. 2018;2(6):527–540.

[24] Frey EC, Tsui B. A new method for modeling the spatially-variant, object-dependent scatter response function in SPECT. In: 1996 IEEE Nuclear Science Symposium. Conference Record. vol. 2. IEEE; 1996. p. 1082–1086.

[25] Dewaraja YK, Frey EC, Sgouros G, Brill AB, Roberson P, Zanzonico PB, et al. MIRD pamphlet no. 23: quantitative SPECT for patient-specific 3-dimensional dosimetry in internal radionuclide therapy. Journal of Nuclear Medicine. 2012;53(8):1310–1325.

[26] Cheng L, Hobbs RF, Segars PW, Sgouros G, Frey EC. Improved dose–volume histogram estimates for radiopharmaceutical therapy by optimizing quantitative SPECT reconstruction parameters. Physics in Medicine & Biology. 2013;58(11):3631.

[27] Cooke DC, Faber TL, Galt JR. Basic sciences of nuclear medicine. Springer Science & Business Media; 2010. Pages 217-255.

# Appendix

## Derivation of optimal sampling time ($t_{opt}$)

If we at time t measure an activity A(t) of a diagnostic radiopharmaceutical with the effective decay constant k=$k_p + \lambda_b$, the time integrated activity for another radiopharmaceutical whose injected activity is a C:th part of the injected diagnostic pharmaceutical is, assuming a mono-exponential behaviour:

$$\tilde{A} = \frac{A(0)}{\lambda} = \frac{C \cdot A_{diag}(0)}{\lambda}, \tag{18}$$

where C is the quota between the injected activity of the therapy radiopharmaceutical and diagnostic radiopharmaceutical or also defined as C=$\frac{1}{A_{inj,diag}}$, and $\lambda = \lambda_p + \lambda_b$ is the effective decay constant of the therapy radiopharmaceutical. Since we can't optimize according to each specific patient we are to use an average value for the biological decay constant based on data from 12 patients, $\lambda_b^*$, hence $k^* = k_p + \lambda_b^*$ and $\lambda^* = \lambda_p + \lambda_b^*$. The time integrated activity then becomes:

$$\tilde{A}^* = \frac{CA(t)e^{k^*t}}{\lambda^*} = \frac{CA(0)e^{-k(t)}e^{k^*t}}{\lambda^*} = \frac{CA(0)}{\lambda^*}e^{(k^*-k)t}. \tag{19}$$

The relative error between the time integrated activity and the average time integrated activity thus becomes:

$$\varepsilon = \frac{\tilde{A}^*}{\tilde{A}} - 1 = \frac{\lambda}{\lambda^*}e^{(k^*-k)t} = \frac{\lambda}{\lambda^*}e^{(\lambda_b^*-\lambda_b)t}, \tag{20}$$

We define t in terms of $\frac{1}{\lambda_b^*} = \tau_b^* \rightarrow t = h \cdot \tau_b^*$. Giving us an relative error where:

$$\varepsilon = \frac{\lambda}{\lambda^*}e^{(\lambda_b^*-\lambda_b)h\cdot\tau_b^*} = \frac{\lambda}{\lambda^*}e^{(1-\frac{\lambda_b}{\lambda_b^*})h} = \frac{\lambda_p+\lambda_b}{\lambda_p+\lambda_b^*}e^{(1-\frac{\lambda_b}{\lambda_b^*})h} \tag{21}$$

We say that e=$\varepsilon^2$ and assume that $\lambda_b^* = E[\lambda_b]$ and then finding the expected value of e:

$$\begin{aligned} E[e(\lambda_b)] &\approx E[e(\lambda_b^*) + \frac{de}{d\lambda}(\lambda_b - \lambda_b^*) + \frac{1}{2}\frac{d^2e}{d\lambda^2}(\lambda_b - \lambda_b^*)^2] = \\ & E[0] + \frac{de}{d\lambda_b}E[\lambda_b - \lambda_b^*] + \frac{1}{2}\frac{d^2e}{d\lambda_b^2}E[(\lambda_b - \lambda_b^*)^2] = \\ \frac{de}{d\lambda_b}E[\lambda_b - E[\lambda_b]] &+ \frac{1}{2}\frac{d^2e}{d\lambda_b^2}E[(\lambda_b - E[\lambda_b])^2] = \frac{1}{2}\frac{d^2e}{d\lambda_b^2}\Big|_{\lambda_b=\lambda_b^*}V[\lambda_b], \end{aligned} \tag{22}$$

where V[·] is the variance. Completing the second derivative gives us:

$$\frac{d^2e}{d\lambda_b^2}\Big|_{\lambda_b=\lambda_b^*} = 2\Big[\frac{\lambda_b^* - h(\lambda_b^*+\lambda_p)}{\lambda_b^*(\lambda_b^*+\lambda_p)}\Big]^2 = 2\Big[\frac{1-h(1+\lambda_p/\lambda_b^*)}{\lambda_b^*+\lambda_p}\Big]^2, \tag{23}$$

and if we let $\frac{\lambda_p}{\lambda_b^*} = m$ then:

$$\frac{d^2e}{d\lambda_b^2}\Big|_{\lambda_b=\lambda_b^*} = 2\Big[\frac{1-h(1+m)}{(1+1/m)\lambda_p^*}\Big]^2 \Rightarrow e \approx \Big[\frac{1-h(1+m)}{1+1/m}\Big]^2 \cdot \frac{V(\lambda_b)}{\lambda_p^2}. \tag{24}$$

We want to find when e has its lowest value since that means our mean TIAC has the smallest uncertainty possible, thus solving $\frac{de}{dh} = 0$,

$$\begin{aligned} \frac{de}{dh} = 2\Big( - \frac{1+m}{1+1/m}\Big) \frac{1-h(1+m)}{1+1/m} \frac{V(\lambda_b)}{\lambda_p^2} = 0 \Leftrightarrow \frac{1-h(1+m)}{1+1/m} = 0 \\ \Leftrightarrow h = \frac{1}{1+m} = \frac{1}{1+\lambda_p/\lambda_b^*} = \frac{\lambda_b^*}{\lambda_b^*+\lambda_p} = \frac{\lambda_b^*}{\lambda^*}. \end{aligned} \tag{25}$$

This gives a minimum, thus e is of second degree with a positive $h^2$-term. The optimal time $t_{opt}$, is then found with:

$$t_{opt} = h_{opt}\tau_s^* = \frac{\lambda_b^*}{\lambda^*}\frac{1}{\lambda_b^*} = \frac{1}{\lambda^*}. \tag{26}$$